Characterizing the tumor microenvironment of metastatic ovarian cancer by single cell transcriptomics.

Susan Olalekan[1*], Bingqing Xie[1], Rebecca Back[1], Heather Eckart[1], Anindita Basu[1,2*]

1 Department of Medicine, University of Chicago
2 Center for Nanoscale Materials, Argonne National Laboratory

*Correspondence:
Anindita Basu, PhD
5841 S. Maryland Avenue. N417B
Chicago, IL 60637
Telephone: 773-834-1512
Fax: 773-702-2567
Email: (onibasu@uchicago.edu)

Running title: scRNA-seq of ovarian cancer tumor microenvironment.

Keywords: Ovarian cancer, scRNA-seq, transcriptomics, immune cells, human cancer

Conflict of interest: The authors declare no potential conflict of interest.

Funding: This project is internally funded.

Abstract

Epithelial ovarian cancer is a highly heterogenous, metastatic and lethal disease. The presence of $CD8^+$T cells within ovarian tumors is positively associated with overall patient survival. Determining if a patient has T cells that respond to immunotherapies, their characteristics and how they can be manipulated to target cancer cells is an area of intense investigation in cancer therapy. This study determines the cellular composition and the transcriptional state of immune cells in metastatic ovarian cancer samples from patients using single cell RNA sequencing (scRNA-seq). Hierarchical clustering stratified our patient cohort into 2 main groups: 1) a high T cell infiltration (high T_{inf}) group and 2) a low T cell infiltration (low T_{inf}) group. To assess the immune response in these patient samples, we performed an unsupervised clustering of the T cell population in each group. The T cell population clustered into 4 and 3 subpopulations in the high T_{inf} T cell and low T_{inf} respectively. A granulysin expressing T cell cluster was identified and unique to the High T_{inf} group. Interestingly, although both groups had resident memory $CD8^+$T ($CD8^+$Trm) cells, only the $CD8^+$Trm cells in the high T_{inf} group expressed TOX, a recently described transcription factor. TOX confers longevity to T cells within immunosuppressive environment such as cancer. Interestingly, along with TOX^+ T cells, we found a unique plasmablast cluster and an $IRF8^+$ macrophage cluster unique to the high T_{inf} group. Our comprehensive scRNA-seq study provides important insights in elucidating the immune response in ovarian cancer patients.

87 # Introduction

88

89 Ovarian cancer is the most lethal malignancy of the female reproductive tract[1]. Conventional
90 therapy involving cytoreductive surgery and chemotherapy are 90% effective when cancer is
91 diagnosed at the early stage when it is still restricted to one or both ovaries. Unfortunately, most
92 ovarian cancer cases are diagnosed at stage III or IV when the cancer has metastasized and the
93 diagnosis in these patients result in a 30% 5-year survival rate[2]. To develop efficacious therapies
94 for metastatic ovarian cancer, we need to define the cellular heterogeneity and the
95 transcriptional state within the tumor microenvironment. Immunohistochemical staining and
96 flow cytometry have been useful in categorizing the cell types based on specific cell surface
97 markers but mask intra-cellular heterogeneity. Bulk RNA profiling has been used to categorize
98 high grade serous ovarian carcinoma (HGSOC), the most common and lethal histotype of ovarian
99 cancer, into molecular subtypes[3,4]. However, bulk RNA sequencing averages gene expression and
100 fails to identify the respective contribution of cell subsets. Alternatively, single cell RNA
101 sequencing (scRNA-seq) has emerged as a powerful tool to interrogate tumor composition,
102 revealing previously uncharacterized cellular heterogeneity and gene regulatory networks at
103 single cell resolution[5-10]. Recently, a scRNA-seq study, investigated the heterogeneity in the
104 proposed cell of origin of HGSOC and revealed a high epithelial-mesenchymal transition (EMT)
105 high subtype associated with poor prognosis[11]. These transcriptomic studies have focused on
106 ovarian cancer cells; however, the tumor microenvironment is made up of other cell types that
107 can affect patient stratification, targeted treatment and outcome.

108

109 The omentum is mainly an adipose tissue in the peritoneal cavity containing aggregates of
110 immune cells in areas called milky spots[12]. These milky spots act similar to lymph nodes, collecting
111 and responding to antigen within the peritoneal cavity. Interestingly, ovarian cancer cells
112 preferentially colonize adipose tissue with milky spots in the peritoneal cavity[13]. Additionally,
113 adipocytes provide adipokines and act as a source of energy for ovarian cancer cells[14]. These
114 factors prime the omentum as a premetastatic niche for ovarian cancer. The initial presence of
115 ovarian cancer cells in the omentum leads to a recruitment of macrophages into the milky spots
116 without anti-tumor effects. Contrastingly, the presence of tumor infiltrating $CD8^+$ T cells in both
117 the ovary and omentum is associated with significantly longer overall survival[15]. However,
118 checkpoint inhibitors, a cancer immunotherapeutic approach, aimed at restoring $CD8^+$ T cell
119 function have had a low response rate[15]. We therefore need a better understanding of the tumor
120 microenvironment to improve patient response rate to cancer immunotherapy.

121

122 In this current study, we use Drop-seq technology to examine the cells within omental tumors
123 from 6 patients with different histotypes of ovarian cancer. We identified 12 cell clusters and
124 patient samples were stratified into two groups based on immune signatures: 1) a high T cell
125 infiltration (high T_{inf}) group and 2) a low T cell infiltration (low T_{inf}) group. This unprecedented
126 concurrent transcriptomic analysis of all cells within metastatic ovarian cancer unravels patient-
127 specific responses to cancer and identifies patients that might be suitable for immune checkpoint
128 inhibition.

129

Materials and methods

Tissue collection

Ovarian cancer tissue was collected from women undergoing debulking surgery at the University of Chicago. Human tissue acquisition after patient deidentification was approved by the university of Chicago institutional review board for human research. Ovarian cancer tissue was histologically carcinoma classified and staged by a pathologist according to tumor-node-metastasis (TMN) and/or international federation of gynecology and obstetrics (FIGO) classifications (Table 1). Three of the ovarian cancer samples originated from the left fallopian tube with associated serous tubal intraepithelial carcinoma (STIC).

Immunohistochemistry

Ovarian cancer tissues obtained from the anatomic pathology department were fixed overnight in 4% formaldehyde at 4^0C. After serial dehydration, the tissues were embedded in paraffin and cut into 5 μm thick sections. Histological evaluation was done with hematoxylin and eosin (H&E). Immunohistochemical staining was performed to confirm the presence of cytokeratin-7 (Thermofisher), pan-vimentin (DAKO), CD45 (Agilent), CD3 (Human Envision) and CD19 (Abcam) cells. Briefly, sections were deparaffinized and rehydrated using xylene and serial dilutions of EtOH in distilled water. Tissue sections were incubated in citrate buffer, pH 6 and heated in a microwave oven. Anti-cytokeratin-7 (1:1000), anti-vimentin (1:100), anti-CD45 (1:100), anti-CD3 (1:100), and anti-CD19 (1:200) antibodies were applied on tissue sections with one-hour incubation at room temperature in a humidity chamber. The antigen-antibody bindings were detected with labeled polymer-HRP Envision system (DAKO, K4007) and DAB+ chromogen (DAKO, K3468) system. Tissue sections were briefly immersed in hematoxylin for counterstaining and were covered with cover glasses.

Tissue digestion, red blood cell lysis and dead cell removal

Ovarian cancer tissue was transported in DMEM/F12 containing 10% FBS and 1% P/S (10% DMEMF/12) on ice from the anatomic pathology department to the laboratory. The tissue was minced manually with a scalpel and enzymatically digested using 1.5 mg/ml collagenase IV (Sigma-Aldrich), 1 mg/ml hyaluronidase (Sigma-Aldrich) and 500 μg/ml DNase I (GoldBio) in Hank's balanced salt solution (HBSS) in a 37 ^{0}C shaker (200 rpm) for 0.5 – 2 h. Following digestion, cells were resuspended in 10% DMEMF/12 and filtered serially through 70 μm and 40 μm strainers. Red blood cells were lysed by incubating the cell suspension in RBC lysis buffer (Sigma-Aldrich) for 2-5 minutes. Lysis was quenched by adding excess 10% DMEMF/12. The number of live cells was enriched using the dead cell removal kit (Miltenyi, 130-090-101).

Drop-seq experiments

172 Drop-seq experiment was performed as previously described[16]. Briefly, cells and barcoded beads
173 were loaded at a concentration of 100,000 cells/ml in PBS-BSA and 120,000 beads/ml in Drop-
174 seq lysis buffer in 3 ml syringes. Droplets were generated using a 125-micron microfluidic device
175 at 16 ml/hr (oil), 4 ml/hr (cells) and 4 ml/hr (beads) with ~15 minutes per collection. Following
176 collection, drops were broken and barcoded beads with mRNA hybridized onto them were
177 collected and washed. Barcoded cDNA attached to the beads or STAMPS were generated by
178 reverse transcription, treated with exonuclease 1 and the number of STAMPs was counted. 5000
179 STAMPSs were aliquoted per well in a 96-well plate and the cDNA attached to the STAMPS were
180 amplified through 14 PCR cycles. Supernatants from each well were pooled and cleaned with
181 Ampure beads. Purified cDNA was quantified using Qubit 3.0 (Invitrogen) and 450-650 pg of each
182 sample was used as input for Nextera reactions (12 cycles). Tagmented libraries were quantified
183 using Agilent BioAnalyzer High sensitivity chip before submission for sequencing on Illumina's
184 NextSeq 500, using 75 cycle v3 kits. Paired end sequencing was performed with 20 bp for Read 1
185 and 64 bp for Read2 using Read1 primer, GCCTGTCCGCGGAAGCAGTGGTATCAACGCAGAGTAC
186 and 5% Illumina PhiX Control v3.
187
188 **Data processing, alignment and clustering analysis**
189
190 From alignment of the reads from the Dropseq experiments, read count matrices for unique
191 molecular identifiers (UMIs) were generated for both exon and intron regions in the human
192 genome (gencode hg38 v.27) using the STAR version 2.5.3 aligner[17,18]. The ovarian cancer samples
193 from six patients' metastatic omentum were sequenced with Drop-seq. A total of 13 sequencing
194 runs were performed for six Drop-seq samples where each sample was sequenced at least twice
195 to maximize the sequencing depth (PT-3401 was sequenced three times). Each run produced
196 paired-end reads, with Read 1 representing the 12 bp cell barcode and six bp unique molecular
197 identifier (UMI), and Read 2 representing a 60 bp mRNA fragment. Paired-end reads from the
198 same samples were merged to generate six paired-end fastq files. A *snakemake* pipeline was
199 applied to each sequencing run and produce a count matrix representing the gene expression in
200 every cell[19]. Individual count matrices were produced for each of the six patients after accounting
201 for UMI duplicates.
202
203 The individual count matrix was produced for each patient with a total number of six count
204 matrices. The summarized counts for each gene were inferred based on both exon and intron
205 reads to produce the gene expression matrix per sample. Expression matrices of six ovarian
206 cancer samples from the metastatic sites in the omentum were generated. To select high quality
207 cells, we applied a filter based on the number of genes detected per cell. Prior to filtering, each
208 sample produced approximately 5000 cells. Based on the median number of genes captured, cells
209 with less than 800 genes were removed from the data sets. For lower quality samples, the
210 threshold was lowered to 600 or 700 as shown in Table 2. We followed a standardized pipeline
211 using single cell analysis tool suite, Seurat v3.0.2[20,21]. A global-scaling logarithmic normalization
212 method was applied to all samples[21] that normalizes the feature expression counts for each cell
213 by the total expression counts, multiplies by a scale factor of 10,000 (TP10K), and natural-log
214 transforms, as ln(TP10K+1). Each normalization matrix was then scaled by a linear transformation
215 to center the mean gene expression of cells and normalized the gene expression variance. The

most variable genes were extracted for principal component analysis (PCA). We applied PCA on the normalized expression matrix with the most variable genes to extract the top 50 components in the data, followed by a heuristic elbow plot on the variance explained of each PC. We selected the number of top variant PCs based on the elbow plot which varies from 10 to 20 depending on the sample. The top PCs were used in further exploration of the data, such as UMAP /tSNE dimension reduction, construction of K-nearest neighbor graph, etc. For analysis that included multiple samples, integration through anchoring[22] was applied. Note that a subset of genes, usually highly variable ones, was selected to perform the integration, where the integrated gene expression matrix has a lesser number of features (genes) than the original gene expression matrix. The samples from multiple patients were integrated before classifying cell types. Differential expression analysis was done through *FindMarkers* function in Seurat V3 using the Wilcoxon Rank Sum test, and statistically significant markers were extracted for sub-populations or contrast groups based on an adjusted p-value threshold of 0.05. We used dimension reduction methods, UMAP[23] and tSNE[24] to generate 2D plots to visualize different cell populations in the experiment.

Cancer subtype classification and correlation with The Cancer Genome Atlas

Four cancer subtypes- differentiated, immunoreactive, mesenchymal, and proliferative were determined from bulk sequencing study on ovarian cancer[4]. Modular scores[25] were generated between gene expression levels for each cell with upregulated marker signatures on the four subtypes. The subtypes were then assigned to individual cells by the highest positive modular score and if no positive modular scores were found, the subtype was considered undecided.

Cell type classification and correlation with CellAtlas

To assign cell types to individual cells, we used a bulk RNA sequencing data-set from 95 cell lines collected by CellAtlas[26], covering 33 major cell types in normal human tissue, including common immune, endothelial, epithelial, fibroblast, mesodermal cells and so on. The cell lines can be further divided into 60 subtypes. We inferred the similarity between individual cells in the samples and cell lines by calculating the pairwise Pearson correlation matrix $C = \{cor(i, j)\}$ among any cell i from the Drop-seq experiments with any cell line, j in the CellAtlas. A shared nearest neighbor (SNN) modularity optimization-based clustering[27] on the CellAtlas cell lines grouped the cell-lines into larger and more general cell-type categories. This was done to eliminate any bias in CellAtlas dataset and remove rare or under-powered cell-types. The resulting clusters of cell-lines were annotated by the most frequent major cell-type from the cell-line groups. For each cell in our cancer sample, cell-type was then assigned from top 5 highly correlated major cell-type clusters. We collapsed ambiguous cell types with neighboring cell types, based on expression profiles.

Classification with cluster markers, canonical genes, and genetic functions

Sometimes the Gene Ontology (GO) and Pathway analysis gives general/noisy functional categories which make certain cell types hard to identify. By leveraging prior knowledge from the CellAtlas mapping, we were able to locate the relevant function categories for those cell types and narrow down their marker genes efficiently[26]. Moreover, by the consensus of both GO and CellAtlas analyses, we obtained higher confidence in classifying cell types in each patient sample.

We used the cell types obtained from CellAtlas correlation as baseline and curated cell-types manually using canonical genes and functional association. Differentially expressed marker genes were extracted from cell clusters. Cross-referencing was done between gene markers and known canonical genes to the cell-types. Gene ontology and pathway enrichment was performed on gene markers to provide additional evidence for cell-type assignment. We identified 9 major cell types including epithelial cells, fibroblast cells, three immune cell types; B cells/B cell plasma, T cells, and monocytes, mesenchymal stem cells (MSC), embryonic stem cells (ESC), and endothelial cells.

Results

Characteristics of the tumor microenvironment

Ovarian cancer samples (1-3 different sections) were collected from the omental metastatic site of six patients (Table 1). Four patients were diagnosed with advanced high-grade serous cancer, one with serous carcinoma and one with malignant mixed Mullerian tumor (MMMT). Ages of the patients ranged from 46 to 71 years. Four of the patients received neo-adjuvant therapy prior to surgery, including the patient diagnosed with MMMT. Normal omentum is comprised mainly of adipocytes as well as aggregates of leukocytes called milky spots[12]. As metastasis progresses, there is an inverse relationship between ovarian tumor growth (cancer and cancer associated cell growth) and adipocytes within the omentum[14]. Therefore, the area of tumor occupied by adipocyte decreases with disease score[28]. To quantify the transformation of the omentum by ovarian cancer cells, we used Imagescope, a digital histopathology software, to annotate and calculate the area occupied by adipocytes in each patient sample on hematoxylin and eosin (H&E) stained sections (Figure 1A). The area of adipocytes was reported as a percentage of the total surface area of the sample and used as a measure of disease score (Figure 1B), similar to Pearce et al.[28] We rated the patient samples from lowest to highest disease score; PT-5150, PT-3401, PT-6885, PT-3232, PT-4806, PT-2834 respectively. The percentage of cancer cells, stromal cells and immune cells were quantified by immunohistochemistry (IHC) using antibodies against cytokeratin-7 (CK-7), vimentin and CD45 antibodies (Figure 1C-H). There was a varying proportion of each cell type across patients. Notably, we observed that malignant cells in some patients (PT-5150, PT- 3232, PT-4806 and PT-2834) double stained for CK-7 and vimentin, suggesting active epithelial-mesenchymal-transition (Figure 1C-F). In addition, the MMMT (PT-2834) sample had two different types of malignant cells that stained separately for CK-7 and vimentin. We assessed the relationship between the area of adipocytes and the cancer and stromal compartments and only observed a positive correlation with $CD45^+$ immune cells (Supplementary Figure 1). Notably,

302 we observed aggregation of immune cells closer to adipocytes and sparsely otherwise
303 throughout the rest of the tissue. Together, these data reveal patient variability in the cellular
304 transformation of tumors from the same pathological stage.
305
306
307 **Generation of single cell data, cell clustering and cell type assignment**
308
309 For Drop-seq experiments, tumors samples were enzymatically digested into a single cell
310 suspension and processed[16]. We integrated all six omental samples into a gene expression matrix
311 which contains the expression values of 9885 cells and 40947 genetic features such as protein
312 coding genes, pseudogenes, lncRNA, mapped from the GENCODE human reference genome
313 (version GRCh38). A minimum cut off of 600-800 genes per cell was set, as shown in Table 2.
314 Hierarchical clustering was performed using resolution of 0.2 with 12 clusters detected
315 (Supplementary Figure 2A). Each cluster had cells from all samples (Supplementary Fig. 2B). The
316 cell types were assigned and curated by cell line correlation, canonical genes and functional
317 categories for the significantly differentially expressed genes on the detected clusters. 9 major
318 clusters out of 12 were identified with cell types (Figure 2A). This included 1 cluster for malignant
319 epithelial cells, 1 cluster for fibroblasts, 1 cluster for mesenchymal stem cells, 1 cluster for
320 embryonic stem cells, 1 cluster for endothelial cells. Each patient sample had a varying proportion
321 of the 9 identified cell types/clusters (Figure 2B). Previous bulk mRNA and microRNA expression
322 studies have established 4 transcriptional subtypes of HGSOC[3,29]. To assign molecular subtypes,
323 we extracted gene sets defining each molecular subtype and applied them to our Drop-seq data.
324 At the single cell level, each molecular subtype is represented in every patient tumor sample
325 (Figure 2C). We further analyzed which cell type/cluster belonged to each molecular subtype.
326 The differentiated and proliferative subtypes were mainly made up of epithelial cells,
327 mesenchymal and immunoreactive subtypes were mainly made up of fibroblasts and immune
328 cells respectively suggesting that TCGA classification is reflective of the proportion of cells types
329 within each tumor (Figure 2D).
330
331 It has been suggested that the TCGA subtypes may be useful in specifically categorizing cancer
332 cells within a tumor. However, most of the cancer cells belonged to the differentiated,
333 proliferative and undecided subtype. Therefore, to determine patient-derived differences in
334 cancer cells that might be useful in personalizing therapy, we generated a heatmap from
335 differentially expressed genes from each patient. The expression profile of all patients appeared
336 similar in all patients except PT-2834 (Figure 2E). This patient was histologically diagnosed with
337 MMMT with chondrosarcomatous elements, also confirmed by our Drop-seq data
338 (Supplementary Figure 3). Next, the central cluster (epithelial cells) and connecting ESCs were
339 selected and assessed for known ovarian cancer cell markers with 7 clusters detected (Figure 2F).
340 PAX8 and MUC16, indicative of advanced disease, was expressed by multiple clusters[30,31]. Cluster
341 1 expressed vimentin along with high Ki-67 and PCLAF indicative of a proliferating population.
342 Cluster 5 also expressed PCLAF, a marker of proliferation, as well as FN1 and ZEB1, markers of
343 EMT. Cluster 6 highly expressed vimentin and Ki-67 along with comparatively lower expression
344 of EMT markers (ZEB1 and ZEB2), suggestive of cells undergoing mesenchymal to epithelial
345 transition (Figure 3E). Ovarian cancer stem cells marked by co-expression of CD33, CD44, CD117

346 and CD24 expression were not observed[32]. Cells in this cluster expressed IL-6 which correlates
347 with poor prognosis in ovarian cancer and TGF-β which induces an aggressive cancer
348 phenotype[33-36]. These results reveal a snapshot of the heterogeneous processes that cancer cells
349 harness to progress disease.
350
351 **Immune cellular profile of patient samples**
352
353 To investigate the immune population in our patient samples, we selected the immune cells from
354 the six patient samples and they clustered into 4 main populations; T cells, B cells, plasma B cells
355 and monocytes/macrophages (Figure 3A). Similar samples were grouped by a dendrogram with
356 a major difference in T cell infiltration (T_{inf}) (Figure 3B). Interestingly, the high T_{inf} group (PT-5150
357 and PT-3401) had the lowest disease score while the low T_{inf} group (PT-4806, PT-6885, PT-2834,
358 PT-3233) had higher disease score. During the initial phase of metastasis, macrophages are
359 recruited from the peritoneal cavity without any anti-tumor effect on the cancer cells[37,38]. To
360 assess the differences in the macrophage population, we performed unsupervised clustering on
361 both groups separately (Figure 3C&D). Both groups had a $CD14^+CD16^+CD163^+CD204^+$ cluster
362 reminiscent of tumor associated macrophages or TAMs (Figure 3E&F, Supplementary Figure 4).
363 In the low T_{inf} group, there was also an immature $FLT3^+$ population. These $FLT3^+$ progenitors can
364 differentiate into osteoclasts, dendritic cells, microglia and macrophages[39]. Other clusters in the
365 high T_{inf} group included a $CD274^+$ cluster, suggesting a regulatory population similar to MDSCs
366 and an $IRF8^+$ cluster induced in the presence of IFN-γ and promotes the formation of
367 autophagosome (Figure 3E&F, Supplementary Figure 4)[40]. The final cluster highly expressed
368 NR1H2 which inhibits inflammatory genes in macrophages[41,42]. This clustering analysis reveals
369 phenotypically distinct macrophages present in the tumor in addition to the established TAMs.
370
371 **Differences in T cell clustering and subtype analysis**
372
373 To reveal the functional subtypes of T cells and any difference in the low T_{inf} versus high T_{inf} group,
374 we clustered 136 and 820 T cells respectively (Figure 5A&B). A total of 3 and 4 transcriptionally
375 distinct clusters emerged from low T_{inf} and high T_{inf} T cells respectively. The top genes revealed
376 clusters similar to previously described T cell phenotypes in breast cancer, including $CD4^+IL7R^+$,
377 $CD4^+FOXP3^+$, resident memory $CD8^+$T cells ($CD8^+$Trm cells) and one population described in lung
378 cancer with high granulysin expression $CD4^+GNLY^+$ (Figure 5C-F, Supplementary Figure 5)[43,44].
379 Both groups had $CD8^+$Trm cells which expressed IFN-γ, $CD4^+IL7R^+$ and $CD4^+FOXP3^+$ T cells. The
380 high T_{inf} group had an extra $CD4^+GNLY^+$ cluster. Contrastingly, GNLY was expressed in the low T_{inf}
381 group by $CD8^+$Trm cluster (Figure 5C&D). TOX was highly expressed by the $CD8^+$Trm and the
382 $CD4^+GNLY^+$ clusters in the high T_{inf} group as compared to the low T_{inf} group (Figure 5E&F). These
383 TOX^+ T cells persist during chronic infection and TOX is expressed on the $CD8^+$T cells that are
384 reactivated in response to PD-L1 immunotherapy[45,46]. Layilin, a previously described marker of
385 exhaustion was mainly expressed by the $CD4^+FOXP3^+$ cluster (Figure 5E&F). These data suggest
386 that scRNA-seq is capable of determining patients that will benefit from novel therapy.
387
388 **Transcriptionally distinct plasmablasts cluster in high T_{inf} group**
389

390 The high T_{inf} group had an accompanying high B cell signature (Figure 3B). To investigate the B
391 cell subtypes in our samples, naïve B cells and plasma cells were clustered yielding 4 and 2
392 clusters in high T_{inf} and low T_{inf} group respectively (Figure 6A&B). In the high and low T_{inf} group,
393 the naïve cluster expressed MHC class II genes highly with a difference in CD24 expression (Figure
394 6C&D, Supplementary Figure 6). Other clusters in both groups expressed BLIMP1 indicating they
395 are plasma cell clusters. In the high T_{inf} group, the BLIMP1$^+$ plasma cells (PC) segregated into 3
396 clusters. The CD38$^+$PC and CD138$^+$PC are indicative of post germinal center B cells. The final
397 cluster highly expressed MHC class II genes as well as proliferative genes suggesting a plasmablast
398 population.
399

400 # Discussion

401
402 In this study, we characterized samples from 6 ovarian cancer patients. One to three sections of
403 tumors were processed to account for intratumor heterogeneity based on availability. Initial IHC
404 staining of these sections revealed a positive correlation between the area of tumor made up of
405 adipocytes and the number of immune cells within the tumor. We processed these tumor
406 sections and obtained Drop-seq data for a total of 9885 cells after quality control. Mapping our
407 cells to curated cell types from the CellAtlas along with gene ontology and pathway-based
408 enrichment was robust in assigning cells types to almost all clusters in our analysis. Our data also
409 revealed a positive correlation between the presence of adipocytes (by IHC) and immune cells
410 and stratified our patient cohort into two groups based on the intrinsic properties of the immune
411 response.
412
413 The largest cluster of cells was cancer epithelial cells, which composed about 50% of cells
414 analyzed. These cells expressed various genes associated with metastatic disease including
415 MUC16 and PAX8, consistent with previous reports. The gene expression matrix was similar
416 between cancer cells from each patient. The variety of cancer associated genes expressed by
417 these cancer cells confirm the compensatory mechanisms that continue to progress disease.
418 Another approach to suppressing tumor growth is by identifying and targeting cancer stem cell
419 (CSC) in ovarian cancer[47]. Like other studies, we were unable to identify cells that expressed
420 known makers of stem cells[48,49]. However, we identified a cell population closely resembling ESC
421 and connected to the epithelial cell cluster that highly expressed proliferative marker, Ki-67.
422 Successful identification for isolation and interrogation of putative ESC might provide useful
423 insight about CSC in ovarian cancer.
424
425 Infiltration of immune cells into the omentum during metastatic cancer does not always elicit
426 anti-tumor responses[38]. In ovarian cancer, high tumor infiltrating T cells is associated with
427 significantly longer overall survival[15]. There is evidence that associates immunogenicity of neo-
428 antigens generated due to high tumor mutational load and clinical response to
429 immunotherapies[50-53]. To this end, we sought to characterize the differences between the two
430 groups in our patient cohort stratified by scRNA-seq data. Macrophages make up 70% of the
431 leukocytes present in the normal omentum so we characterized them first. Although TAMs were
432 found in both groups, an extra 2 clusters expressing NR1H2 and CD274 were found in the high

433 T_{inf} group. Both these markers are upregulated in an activation dependent manner suggesting
434 that the high T_{inf} group is actually mounting an anti-tumor immune response. Flt3$^+$ progenitors
435 were unique to the low T_{inf} group. Along with the presence of TAMs, these data suggest that
436 macrophages in the low T_{inf} group acquired immunosuppressive phenotype in response to the
437 presence of cancer cells.
438
439 Advances in personalized medicine has revealed TOX as a transcription factor expressed by T cells
440 that respond to immune checkpoint block[45,54]. In our patient cohort, TOX was mainly expressed
441 by two T cell clusters, CD8$^+$Trm and CD4$^+$GNLY in the high T_{inf} group. The low T_{inf} group also had
442 the CD8$^+$Trm subset which expressed granulysin but not a separate CD4$^+$GNLY subset.
443 Interestingly, there was minimal TOX expression in the low T_{inf} group. Layilin, a marker gene
444 expressed by exhausted CD8$^+$T cells and regulatory T cells, was mainly expressed by the
445 CD4$^+$FOXP3$^+$ cluster in our study. Only a few CD8$^+$T cells expressed Layilin. Coincidentally, there
446 is also a difference in the B cell population between the low and high T_{inf} groups. Along with the
447 expression of TOX in T cells, the high T cell response group also had a unique subset of
448 BLIMP1$^+$CD38$^+$CD138$^+$ B cells and plasmablasts. It is likely that antigen-cognate plasmablasts are
449 involved in the generation or maintenance of TOX$^+$ T cells. A mechanistic study of these cells is
450 necessary as they may hold the key into inducing TOX$^+$T cells in patients who do not respond to
451 immune checkpoint inhibitors.
452
453 In addition to the major cell types analyzed, there were other clusters including 3 undecideds
454 (N1, N2, N3), 1 endothelial, 1 mesenchymal stem cell and 1 fibroblast cluster. For the undecided
455 clusters, by mapping them to the CellAtlas cell types, they best correlate with astrocytes,
456 CMP/bone marrow progenitor and plasmacytoid dendritic cells respectively. We did not recover
457 adipocytes as they were probably lost during the tissue dissociation. Endothelial cells are the
458 major cell types involved in angiogenesis which is necessary for metastasis. The mesenchymal
459 stem cells are connected to the fibroblasts. Inflamed omentum contains stem cells displaying
460 similar surface markers to MSCs. These stem cells are capable of differentiating into fat, cartilage
461 or bone depending on the secreted factors present[55,56]. Finally, there was a significant fibroblast
462 cluster in our sample population. Metastatic transformation of the omentum changes the cellular
463 composition from mainly adipocytes to cancer cells, immune cells and fibroblasts[28]. Cancer
464 associated fibroblasts mainly function to remodel the extracellular matrix in the tumor
465 microenivironment[57]. Recently, a scRNA-seq study of CAF in pancreatic cancer revealed a
466 LRRC15$^+$ CAF population that correlated with poor response in patients treated with anti-PD-L1
467 therapy[58]. A few of the fibroblasts in our study also express LRRC15 (data not shown). Ultimately,
468 more studies are needed to further elucidate these cells and how they can be manipulated to
469 enhance immunotherapeutic approaches.
470

471 # Conclusion

472
473 To our knowledge, this is the first scRNA-seq study that allows stratification of patient samples
474 all initially pathologically classified as stage III, according to immune response in metastatic
475 ovarian cancer. Concurrent transcriptomic analysis of cancer and stromal cells revealed patient

heterogeneity highlighting the need for personalized medicine. Interrogating tumor infiltrating lymphocytes at the single cell level also revealed patient-intrinsic responses that are previously undescribed in ovarian cancer. Mechanistic studies are required to determine the role of these cells in tumor progression and response to novel cancer immunotherapies.

Acknowledgment

We are grateful to Drs. Mengjie Chen and Ernst Lengyel for helpful discussions and Mark Lingen for tissue access. All tissues were histologically graded, de-identified and obtained from the University of Chicago Human Tissue Resource Center. Computational resources and data storage were provided by the University of Chicago Research Computing Center. This work was performed, in part, at the Center for Nanoscale Materials, a U.S. Department of Energy Office of Science User Facility, and supported by the U.S. Department of Energy, Office of Science, under Contract No. DE-AC02-06CH11357.

References

1 Siegel, R. L., Miller, K. D. & Jemal, A. Cancer Statistics, 2017. *CA: a cancer journal for clinicians* **67**, 7-30, doi:10.3322/caac.21387 (2017).

2 Testa, U., Castelli, G. & Pelosi, E. Genetic Abnormalities, Clonal Evolution, and Cancer Stem Cells of Brain Tumors. *Med Sci (Basel)* **6**, doi:10.3390/medsci6040085 (2018).

3 Tothill, R. W. *et al.* Novel molecular subtypes of serous and endometrioid ovarian cancer linked to clinical outcome. *Clinical cancer research : an official journal of the American Association for Cancer Research* **14**, 5198-5208, doi:10.1158/1078-0432.CCR-08-0196 (2008).

4 Network, C. G. A. R. Integrated genomic analyses of ovarian carcinoma. *Nature* **474**, 609 (2011).

5 Zheng, G. X. *et al.* Massively parallel digital transcriptional profiling of single cells. *Nat Commun* **8**, 14049, doi:10.1038/ncomms14049 (2017).

6 Villani, A. C. *et al.* Single-cell RNA-seq reveals new types of human blood dendritic cells, monocytes, and progenitors. *Science* **356**, doi:10.1126/science.aah4573 (2017).

7 Dixit, A. *et al.* Perturb-Seq: Dissecting Molecular Circuits with Scalable Single-Cell RNA Profiling of Pooled Genetic Screens. *Cell* **167**, 1853-1866 e1817, doi:10.1016/j.cell.2016.11.038 (2016).

8 Jaitin, D. A. *et al.* Dissecting Immune Circuits by Linking CRISPR-Pooled Screens with Single-Cell RNA-Seq. *Cell* **167**, 1883-1896 e1815, doi:10.1016/j.cell.2016.11.039 (2016).

9 Shalek, A. K. *et al.* Single-cell transcriptomics reveals bimodality in expression and splicing in immune cells. *Nature* **498**, 236-240, doi:10.1038/nature12172 (2013).

10 Zheng, C. *et al.* Landscape of Infiltrating T Cells in Liver Cancer Revealed by Single-Cell Sequencing. *Cell* **169**, 1342-1356 e1316, doi:10.1016/j.cell.2017.05.035 (2017).

11 Hu, Z. *et al.* The Repertoire of Serous Ovarian Cancer Non-genetic Heterogeneity Revealed by Single-Cell Sequencing of Normal Fallopian Tube Epithelial Cells. *Cancer cell* **37**, 226-242 e227, doi:10.1016/j.ccell.2020.01.003 (2020).
12 Platell, C., Cooper, D., Papadimitriou, J. M. & Hall, J. C. The omentum. *World J Gastroenterol* **6**, 169-176, doi:10.3748/wjg.v6.i2.169 (2000).
13 Clark, R. *et al.* Milky spots promote ovarian cancer metastatic colonization of peritoneal adipose in experimental models. *The American journal of pathology* **183**, 576-591, doi:10.1016/j.ajpath.2013.04.023 (2013).
14 Nieman, K. M. *et al.* Adipocytes promote ovarian cancer metastasis and provide energy for rapid tumor growth. *Nature medicine* **17**, 1498-1503, doi:10.1038/nm.2492 (2011).
15 Santoiemma, P. P. & Powell, D. J., Jr. Tumor infiltrating lymphocytes in ovarian cancer. *Cancer Biol Ther* **16**, 807-820, doi:10.1080/15384047.2015.1040960 (2015).
16 Macosko, E. Z. *et al.* Highly Parallel Genome-wide Expression Profiling of Individual Cells Using Nanoliter Droplets. *Cell* **161**, 1202-1214, doi:10.1016/j.cell.2015.05.002 (2015).
17 Frankish, A. *et al.* GENCODE reference annotation for the human and mouse genomes. *Nucleic Acids Res* **47**, D766-D773, doi:10.1093/nar/gky955 (2019).
18 Dobin, A. *et al.* STAR: ultrafast universal RNA-seq aligner. *Bioinformatics* **29**, 15-21, doi:10.1093/bioinformatics/bts635 (2013).
19 Selewa, A. *et al.* Systematic Comparison of High-throughput Single-Cell and Single-Nucleus Transcriptomes during Cardiomyocyte Differentiation. *BioRxiv*, doi:10.1101/585901 (2019).
20 Butler, A., Hoffman, P., Smibert, P., Papalexi, E. & Satija, R. Integrating single-cell transcriptomic data across different conditions, technologies, and species. *Nature biotechnology* **36**, 411-420, doi:10.1038/nbt.4096 (2018).
21 Stuart, T. *et al.* Comprehensive Integration of Single-Cell Data. *Cell* **177**, 1888-1902 e1821, doi:10.1016/j.cell.2019.05.031 (2019).
22 Stuart, T. *et al.* Comprehensive Integration of Single-Cell Data. *Cell* **177**, 1888-1902 (2019).
23 McInnes, L., Healy, J. & Melville, J. UMAP: Uniform Manifold Approximation and Projection for Dimension Reduction. *Journal of Open Source Software* **29**, 861, doi:https://doi.org/10.21105/joss.00861 (2018).
24 Maaten, L. v. d. & Hinton, G. isualizing data using t-SNE. *Journal of machine learning research 9* **9**, 2579-2605 (2008).
25 I, T. *et al.* Dissecting the multicellular ecosystem of metastatic melanoma by single-cell RNA-seq. *Science* **352**, 189-196 (2016).
26 Mabbott, N. A., Baillie, J. K., Brown, H., Freeman, T. C. & Hume, D. A. An expression atlas of human primary cells: inference of gene function from coexpression networks. *BMC Genomics* **14**, 632, doi:10.1186/1471-2164-14-632 (2013).
27 Waltman, L. & Eck, N. J. V. A smart local moving algorithm for large-scale modularity-based community detection. *The European physical journal B* **86**, 471 (2013).
28 Pearce, O. M. T. *et al.* Deconstruction of a Metastatic Tumor Microenvironment Reveals a Common Matrix Response in Human Cancers. *Cancer Discov* **8**, 304-319, doi:10.1158/2159-8290.CD-17-0284 (2018).
29 Network., C. G. A. R. Intergrated genomic analyses of ovarian carcinoma. *Nature* **474**, 609-615, doi:https://doi.org/10.1038/nature10166 (2011).

562 30 Robertson, D. M. *et al.* Combined inhibin and CA125 assays in the detection of ovarian
563 cancer. *Clin Chem* **45**, 651-658 (1999).
564 31 Theriault, C. *et al.* MUC16 (CA125) regulates epithelial ovarian cancer cell growth,
565 tumorigenesis and metastasis. *Gynecologic oncology* **121**, 434-443,
566 doi:10.1016/j.ygyno.2011.02.020 (2011).
567 32 Klemba, A. *et al.* Surface markers of cancer stem-like cells of ovarian cancer and their
568 clinical relevance. *Contemp Oncol (Pozn)* **22**, 48-55, doi:10.5114/wo.2018.73885 (2018).
569 33 Coward, J. *et al.* Interleukin-6 as a therapeutic target in human ovarian cancer. *Clinical*
570 *cancer research : an official journal of the American Association for Cancer Research* **17**,
571 6083-6096, doi:10.1158/1078-0432.CCR-11-0945 (2011).
572 34 Lutgendorf, S. K. *et al.* Interleukin-6, cortisol, and depressive symptoms in ovarian cancer
573 patients. *Journal of clinical oncology : official journal of the American Society of Clinical*
574 *Oncology* **26**, 4820-4827, doi:10.1200/JCO.2007.14.1978 (2008).
575 35 Scambia, G. *et al.* Prognostic significance of interleukin 6 serum levels in patients with
576 ovarian cancer. *Br J Cancer* **71**, 354-356, doi:10.1038/bjc.1995.71 (1995).
577 36 Li, W. *et al.* TGFbeta1 in fibroblasts-derived exosomes promotes epithelial-mesenchymal
578 transition of ovarian cancer cells. *Oncotarget* **8**, 96035-96047,
579 doi:10.18632/oncotarget.21635 (2017).
580 37 Shimotsuma, M., Simpson-Morgan, M. W., Takahashi, T. & Hagiwara, A. Activation of
581 omental milky spots and milky spot macrophages by intraperitoneal administration of a
582 streptococcal preparation, OK-432. *Cancer research* **52**, 5400-5402 (1992).
583 38 Oosterling, S. J. *et al.* Insufficient ability of omental milky spots to prevent peritoneal
584 tumor outgrowth supports omentectomy in minimal residual disease. *Cancer Immunol*
585 *Immunother* **55**, 1043-1051, doi:10.1007/s00262-005-0101-y (2006).
586 39 Servet-Delprat, C. *et al.* Flt3+ macrophage precursors commit sequentially to osteoclasts,
587 dendritic cells and microglia. *BMC Immunol* **3**, 15, doi:10.1186/1471-2172-3-15 (2002).
588 40 Gupta, M. *et al.* IRF8 directs stress-induced autophagy in macrophages and promotes
589 clearance of Listeria monocytogenes. *Nat Commun* **6**, 6379, doi:10.1038/ncomms7379
590 (2015).
591 41 Castrillo, A., Joseph, S. B., Marathe, C., Mangelsdorf, D. J. & Tontonoz, P. Liver X receptor-
592 dependent repression of matrix metalloproteinase-9 expression in macrophages. *J Biol*
593 *Chem* **278**, 10443-10449, doi:10.1074/jbc.M213071200 (2003).
594 42 N, A. G. & Castrillo, A. Liver X receptors as regulators of macrophage inflammatory and
595 metabolic pathways. *Biochim Biophys Acta* **1812**, 982-994,
596 doi:10.1016/j.bbadis.2010.12.015 (2011).
597 43 Savas, P. *et al.* Publisher Correction: Single-cell profiling of breast cancer T cells reveals a
598 tissue-resident memory subset associated with improved prognosis. *Nature medicine* **24**,
599 1941, doi:10.1038/s41591-018-0176-6 (2018).
600 44 Guo, X. *et al.* Publisher Correction: Global characterization of T cells in non-small-cell lung
601 cancer by single-cell sequencing. *Nature medicine* **24**, 1628, doi:10.1038/s41591-018-
602 0167-7 (2018).
603 45 Yao, C. *et al.* Single-cell RNA-seq reveals TOX as a key regulator of CD8(+) T cell persistence
604 in chronic infection. *Nat Immunol* **20**, 890-901, doi:10.1038/s41590-019-0403-4 (2019).

605 46 Khan, O. *et al.* TOX transcriptionally and epigenetically programs CD8(+) T cell exhaustion.
606 *Nature* **571**, 211-218, doi:10.1038/s41586-019-1325-x (2019).
607 47 Bast, R. C., Jr., Hennessy, B. & Mills, G. B. The biology of ovarian cancer: new opportunities
608 for translation. *Nat Rev Cancer* **9**, 415-428, doi:10.1038/nrc2644 (2009).
609 48 Shah, M. M. & Landen, C. N. Ovarian cancer stem cells: are they real and why are they
610 important? *Gynecologic oncology* **132**, 483-489, doi:10.1016/j.ygyno.2013.12.001 (2014).
611 49 Burgos-Ojeda, D., Rueda, B. R. & Buckanovich, R. J. Ovarian cancer stem cell markers:
612 prognostic and therapeutic implications. *Cancer letters* **322**, 1-7,
613 doi:10.1016/j.canlet.2012.02.002 (2012).
614 50 Van Allen, E. M. *et al.* Genomic correlates of response to CTLA-4 blockade in metastatic
615 melanoma. *Science* **350**, 207-211, doi:10.1126/science.aad0095 (2015).
616 51 Rizvi, N. A. *et al.* Cancer immunology. Mutational landscape determines sensitivity to PD-
617 1 blockade in non-small cell lung cancer. *Science* **348**, 124-128,
618 doi:10.1126/science.aaa1348 (2015).
619 52 Snyder, A. *et al.* Genetic basis for clinical response to CTLA-4 blockade in melanoma. *N*
620 *Engl J Med* **371**, 2189-2199, doi:10.1056/NEJMoa1406498 (2014).
621 53 Aguade-Gorgorio, G. & Sole, R. Genetic instability as a driver for immune surveillance. *J*
622 *Immunother Cancer* **7**, 345, doi:10.1186/s40425-019-0795-6 (2019).
623 54 Siddiqui, I. *et al.* Intratumoral Tcf1(+)PD-1(+)CD8(+) T Cells with Stem-like Properties
624 Promote Tumor Control in Response to Vaccination and Checkpoint Blockade
625 Immunotherapy. *Immunity* **50**, 195-211 e110, doi:10.1016/j.immuni.2018.12.021 (2019).
626 55 Shah, S. *et al.* Cellular basis of tissue regeneration by omentum. *PloS one* **7**, e38368,
627 doi:10.1371/journal.pone.0038368 (2012).
628 56 Friedenstein, A. J., Petrakova, K. V., Kurolesova, A. I. & Frolova, G. P. Heterotopic of bone
629 marrow. Analysis of precursor cells for osteogenic and hematopoietic tissues.
630 *Transplantation* **6**, 230-247 (1968).
631 57 Kalluri, R. The biology and function of fibroblasts in cancer. *Nat Rev Cancer* **16**, 582-598,
632 doi:10.1038/nrc.2016.73 (2016).
633 58 Dominguez, C. X. *et al.* Single-Cell RNA Sequencing Reveals Stromal Evolution into
634 LRRC15(+) Myofibroblasts as a Determinant of Patient Response to Cancer
635 Immunotherapy. *Cancer Discov* **10**, 232-253, doi:10.1158/2159-8290.CD-19-0644 (2020).
636

Table 1. De-identified meta-data for all omental tumors collected from ovarian cancer patients.

Omentum	Age	Race	Origin	Histologic type	Histological grade	Neoadjuvant therapy	Stage (PMN/FIGO)
PT-3232	46	Asian	Left fallopian (STIC)	High grade serous carcinoma	High grade	No	pT3c Nx / IIIc
PT-3401	56	White	Left ovary	High grade serous carcinoma	High grade	No	pT3c Nx Mx/ IIIc
PT-6885	66	Black	Left fallopian (STIC)	High grade serous carcinoma	High grade	Yes	ypT3c N1a / IIIc
PT-5150	62	White	undetermined	Serous	Not applicable	Yes	ypT3a Nx M1/ Ivb
PT-2834	66	Asian	Fallopian	Malignant mixed Mullerian tumor	High grade	Yes	ypT3c Nx/ IIIc
PT-4806	71	Black	Left fallopian (STIC)	High grade serous carcinoma	High grade	Yes	pT3c, N1, M1/ IIIc

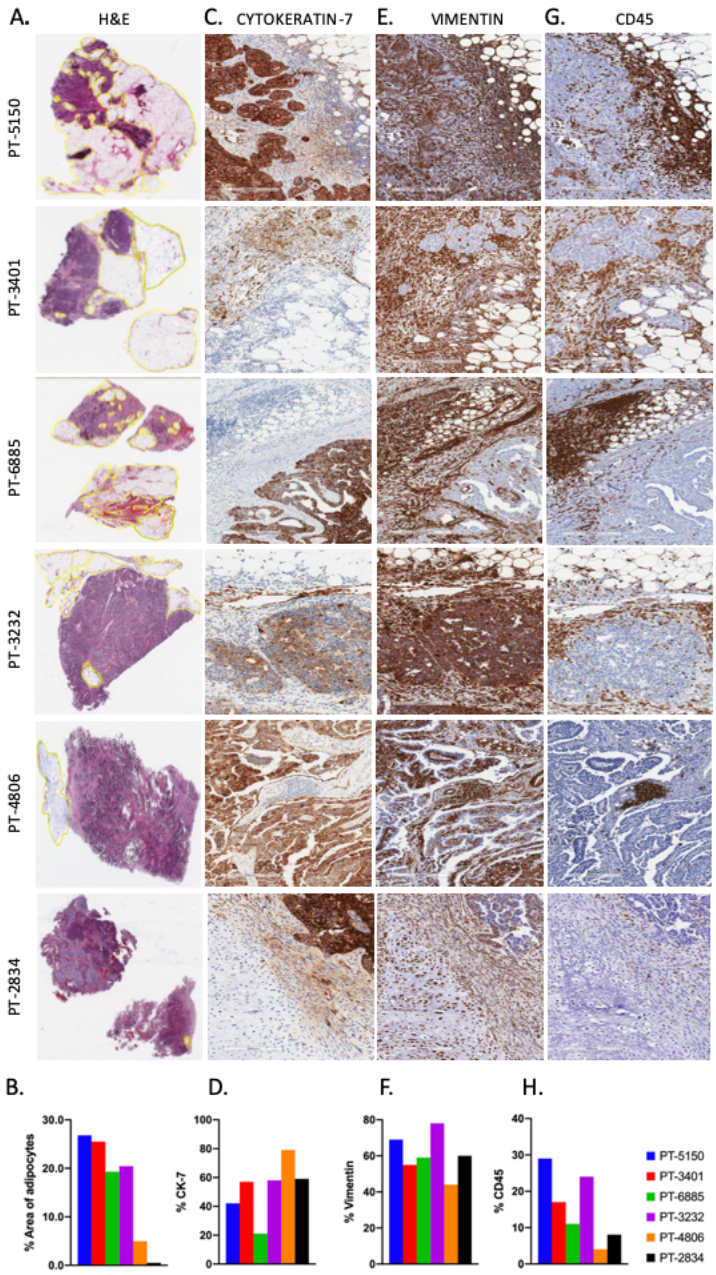

Figure 1. Immunohistochemical staining and sample description. A) The hematoxylin and eosin (H&E) stained sections with B) the histogram of percentage area of adipocytes on the patient sample. C) Cytokeratin-7 (CK-7) staining on patient sample with D) histogram of the percentage of CK-7 positive cells. E) Vimentin staining on patient sample with F) the histogram of percentage of Vimentin positive cells. G) CD45 staining on patient sample with H) histogram of the percentage of CD45 positive cells. Images were taken at A) 40x; C), E), G) 400x.

Table 2. Filter parameters applied to samples collected from six patients and the resulting number of cells and genes per sample.

	Gene Cutoff	No of Genes	No of Cells
PT-5150	600	24776	1244
PT-3401	800	32024	3451
PT-6885	800	24063	1071
PT-3232	700	19297	1102
PT-4806	700	26499	1108
PT-2834	800	26221	1909

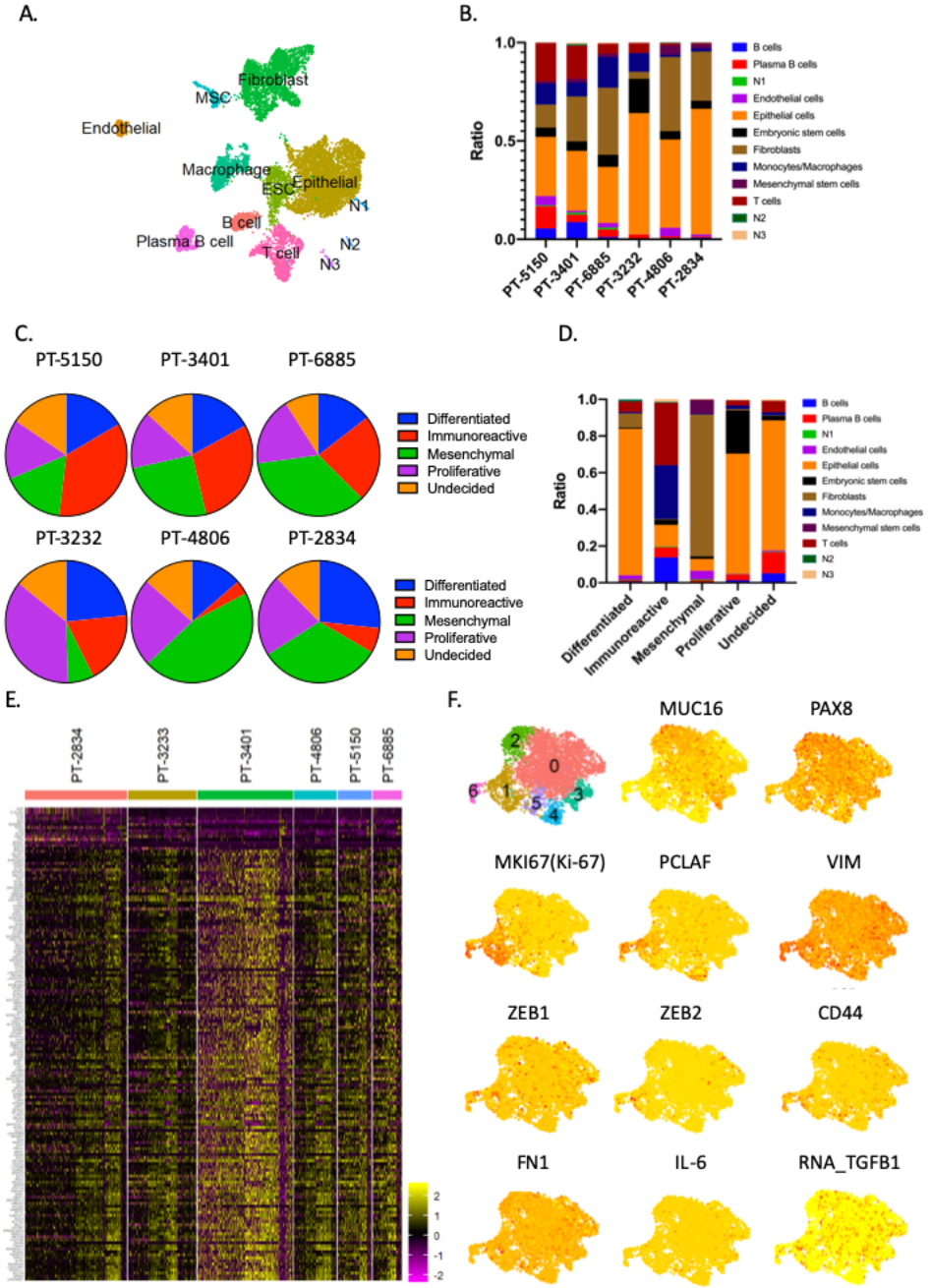

Figure 2. Cell and molecular subtypes assignment using Drop-seq data. A) UMAP plot for high-quality cells, based on number of genes detected per cell in all six omentum samples, colored by clustering results. B) Ratio of cellular composition by patients. C) Cancer subtype designation for each patient sample based on TCGA. D) Cancer subtype designation by cell type based on TCGA. E) Heatmap of top 150 genes for single cells (cancer and ESCs) in each patient sample. F) UMAP and feature plots of relevant marker genes of 4733 annotated cancer cell-types only from all six omentum.

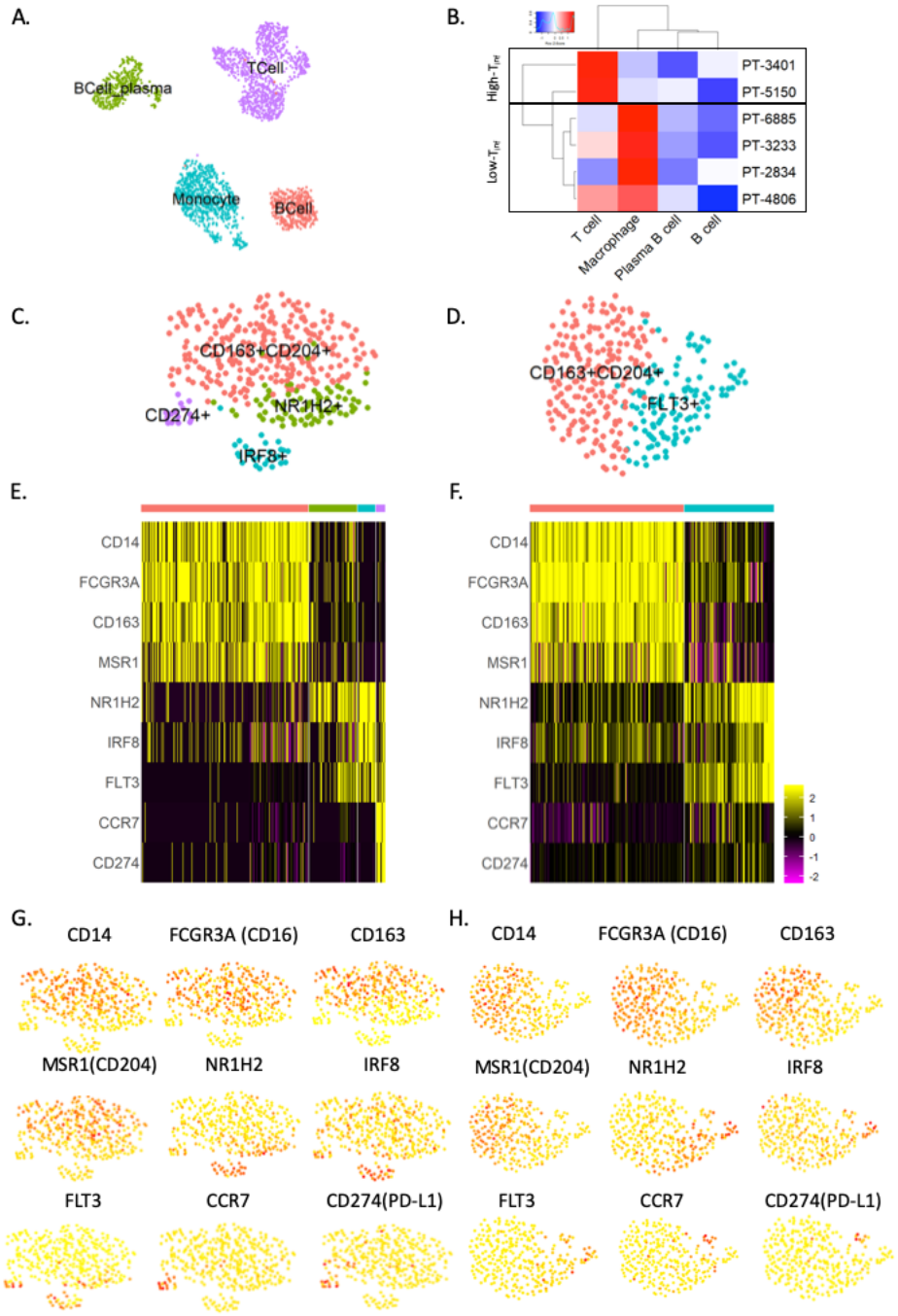

Figure 3. scRNA-seq of annotated immune population from omental tumors. A) UMAP plot separated by colors showing the 4 main immune cell-types based on correlation with Cell Atlas cell-type. B) Heatmap of immune cell types (T cell, B cell, plasma B cell, and Monocyte) in each patient sample with dendrograms on cell types (columns) and patients (rows), dividing the samples into high and low T cell infiltration groups. C & D) UMAP plots of unsupervised clustering of annotated macrophages from C) high T_{inf} (383 cells), and D) low T_{inf} (312 cells) groups. Heat maps from single cell analysis showing differentially expressed markers between clusters in the two groups: E) high T_{inf}, and F) low T_{inf} group. G&H) Feature plots demonstrating expression of relevant genes in macrophages in high and low high T_{inf} groups, respectively.

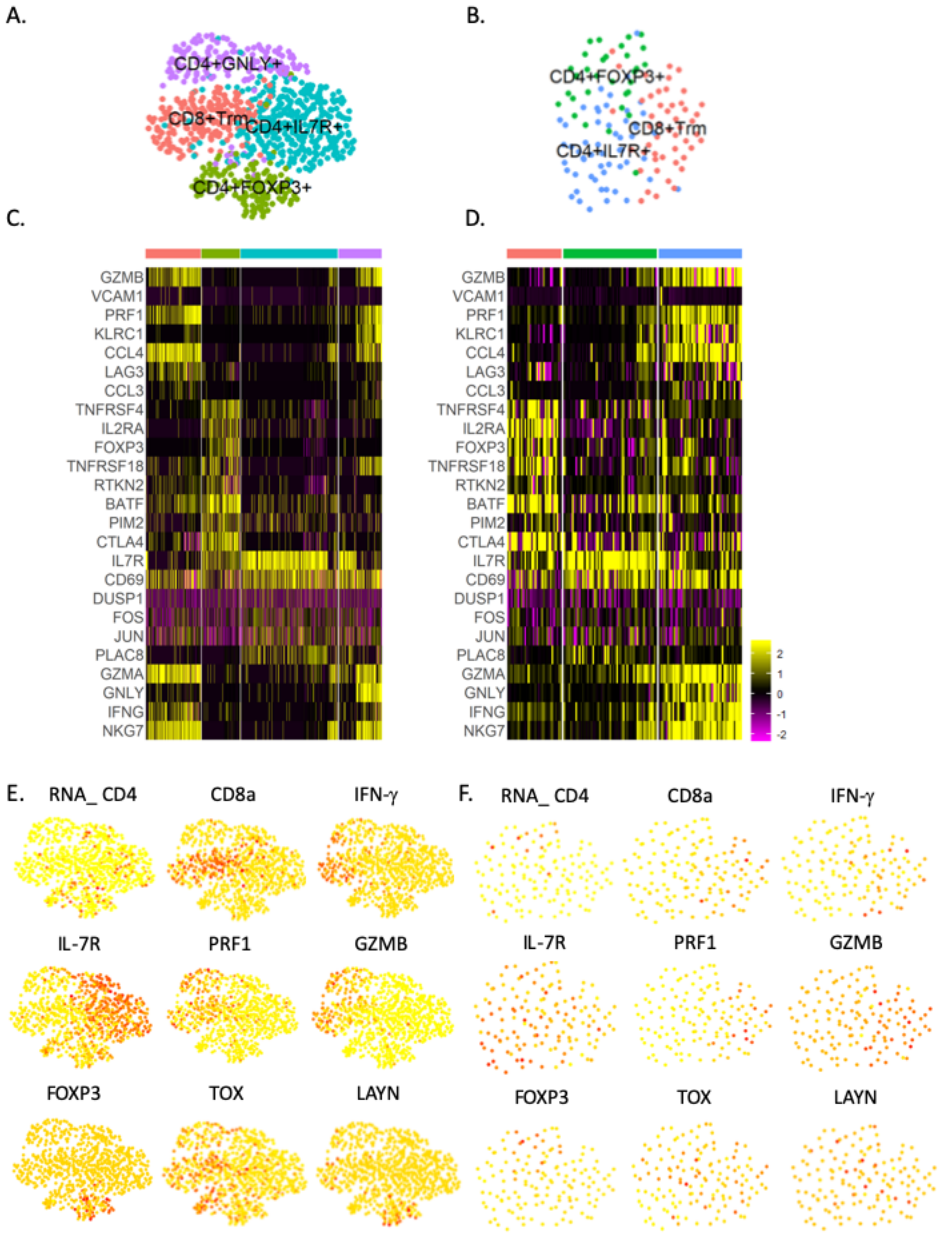

Figure 4. Characterization of annotated T cell population. UMAP plot for T cells in A) high T_{inf} (820 cells), and B) low T_{inf} (136) group. Heat maps from single-cell analysis of key genes in different clusters in C) high T_{inf}, and D) low T_{inf} groups. Clusters in heat map are indicated by the same color as in the UMAP plots. Feature plots showing expression of key genes in E) high T_{inf}, and F) low T_{inf} groups.

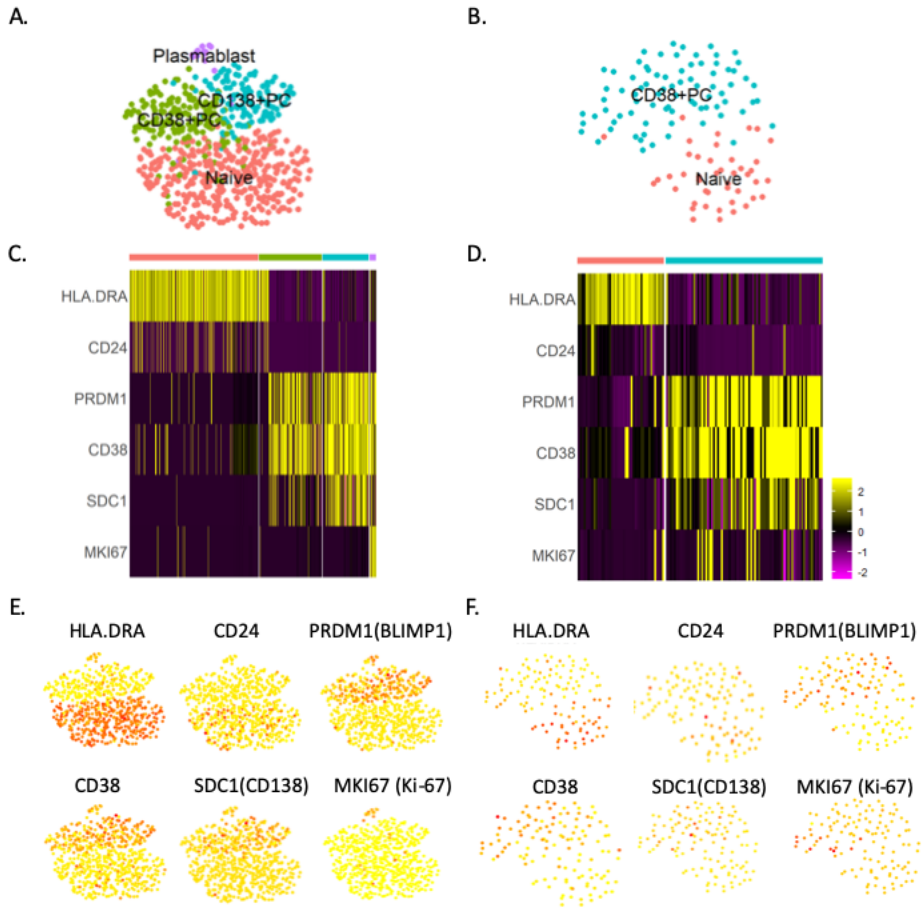

Figure 5. Identification of B cell clusters using single cell analysis. UMAP plot for B cells in A) high T_{inf} (396 cells) and B) low T_{inf} (124 cells) groups. Heat maps from single-cell analysis of key genes in different clusters in C) high T_{inf}, and D) low T_{inf} groups. Clusters in heat map are indicated by the same color as in the UMAP plots. Feature plots showing expression of key genes in E) high T_{inf}, and F) low T_{inf} groups.